ARTICLE

Three-dimensional porous platinum-tellurium-rhodium surface/interface achieve remarkable practical fuel cell catalysis

Received 00th January 20xx,
Accepted 00th January 20xx

DOI: 10.1039/x0xx00000x

Lingzheng Bu[a,*], Fandi Ning[b], Jing Zhou[c], Changhong Zhan[a], Mingzi Sun[d], Leigang Li[a], Yiming Zhu[e], Zhiwei Hu[f], Qi Shao[e], Xiaochun Zhou[b], Bolong Huang[d,*], and Xiaoqing Huang[a,*]

Engineering high-efficiency surfaces/interfaces in electrocatalyst is critical for fuel cell commercialization. Herein, we construct a class of porous PtTeRh nanorods (NRs) with three-dimensional surfaces/interfaces for efficient oxygen reduction reaction (ORR) catalysts for practical fuel cells. The optimized porous $Pt_{61}Te_8Rh_{31}$ NRs/C exhibits 14-fold improvements in the ORR kinetics and remarkable self-breathing membrane electrode assembly (MEA) performance (normalized power density of 1023.8 W g^{-1}_{Pt}, only 1.3% cell voltage loss after 240 h durability test). Even under harsh operating fuel cell conditions, it can readily achieve a much higher power density (1976.1 mW cm^{-2}) than commercial Pt/C (1338.8 mW cm^{-2}). Simultaneously, it showed 14.2% loss in peak power density after 30000 cycles of accelerated stress test (AST), while commercial Pt/C exhibited 25.7% peak power density loss under the same test condition, demonstrating a highly active and durable cathodic catalyst for MEA. Density functional theory (DFT) calculations reveal the converse redox trend for Pt and Rh sites for optimizing the electron transfer during the ORR process. Te activates the strong *p-d* couplings and preserves the robust electroactivity for superior electroactivity and durability. This work represents a significant advance in rationally designing multicomponent nanomaterials for practical fuel cell applications.

Introduction

Compared with different anodic reactions in various fuel cells and metal-air batteries, cathodic oxygen reduction reaction (ORR) plays a more decisive role in the contribution of device capability due to its relatively sluggish kinetics[1-4]. Applying efficient catalysts in these systems can effectively drive ORR to achieve satisfactory kinetics through reducing reaction activation energy. By far, platinum (Pt)-based nanomaterials are widely used as the high-performance ORR catalysts[5-9]. However, it is still a long way to go before realizing the large-scale commercialization of Pt-based catalysts under the comprehensive consideration of cost, storage, catalytic property, and practical feasibility[10-13]. Therefore, developing a class of cost-effective and high-efficiency Pt-based catalysts for ORR and further reaching the superior membrane electrode assembly (MEA) performance in proton exchange membrane fuel cell (PEMFC) is of great importance.

Under practical operating conditions, many parameters (activity, lifetime, ionomer distribution, active site density, the stuffed state in cells, physical and chemical structures, graphitization degree and porosity of carbon support, the interaction between catalyst and support, etc.) can affect the performances of fuel cells[14-18], which provides us important inspirations to optimize the oxygen reduction catalysis. Take the state-of-the-art commercial Pt/C as an example, it usually displays relatively poor activity and stability in ORR and operating fuel cells because of its demerits in structure, dimensionality, composition, and so on. From the perspective of structure design, small-sized Pt nanoparticles (NPs) with zero-dimension (0D) may have many active sites on the surface, but with poor anti-deformation ability due to their structural shortcomings. During the long-term catalysis process, 0D Pt-based NPs readily undergo serious aggregation and size change, leading to the loss of active sites and degradation of MEA performance[19]. By contrast, the 1D Pt-based nanostructures possess diversified merits for achieving superior catalytic performance, including anisotropic morphology, high conductivity, high flexibility, strong interaction with support, and so forth[20-22]. On the other hand, constructing highly open Pt-based nanostructures, such as porous nanomaterials (PNMs)[23], nanocages (NCs)[24], and nanoframes (NFs)[25], has been demonstrated as an effective strategy to furthest increase the density of active sites and improve the reaction kinetics[26]. This is not only because that a large number of interior atoms can be

[a]*State Key Laboratory of Physical Chemistry of Solid Surfaces, College of Chemistry and Chemical Engineering, Xiamen University, Xiamen, Fujian 361005, P. R. China.*
[b]*Division of Advanced Nanomaterials, Suzhou Institute of Nano-Tech and Nano-Bionics, Chinese Academy of Sciences (CAS), Suzhou, Jiangsu 215123, P. R. China.*
[c]*Key Laboratory of Interfacial Physics and Technology, Shanghai Institute of Applied Physics, Chinese Academy of Sciences (CAS), Shanghai 201800, P. R. China.*
[d]*Department of Applied Biology and Chemical Technology, The Hong Kong Polytechnic University, Hung Hom, Kowloon, Hong Kong SAR, P. R. China.*
[e]*College of Chemistry, Chemical Engineering and Materials Science, Soochow University, Suzhou, Jiangsu 215123, P. R. China.*
[f]*Max Planck Institute for Chemical Physics of Solids, Nothnitzer Strasse 40, Dresden 01187, Germany.*
[*]Correspondence to: lzbu@xmu.edu.cn; bhuang@polyu.edu.hk; hxq006@xmu.edu.cn
Electronic Supplementary Information (ESI) available: [details of any supplementary information available should be included here]. See DOI: 10.1039/x0xx00000x

exposed to contribute to the enhanced catalysis, but also due to that the presence of numerous active stepped atoms located on/at the surfaces/interfaces can further improve the catalytic activity, collectively giving rise to the maximized Pt utilization efficiency. Based on the overall considerations, rationally engineering open surface/interface configurations in anisotropic 1D Pt-based nanomaterials may achieve a class of active and stable catalysts for practical fuel cell catalysis, but it remains a formidable challenging subject to date.

Herein, for the first time, a class of novel porous Pt-tellurium-rhodium nanorods (porous PtTeRh NRs) with 1D building block and 3D open surface/interface were designed as the high-efficiency cathodic ORR electrocatalysts for PEMFC in both self-breathing and operating fuel cell media. These unique porous architectures originate from the initially-constructed spongy PtTeRh NRs with controlled compositions through a consequent chemical and electrochemical ageing (CCEA) strategy. The resulting optimized porous $Pt_{61}Te_8Rh_{31}$ NRs/C displays the highest ORR specific and mass activities of 4.4 mA cm^{-2} and 2.4 A mg^{-1}_{Pt} at 0.90 V versus reversible hydrogen electrode (vs. RHE), which are 17.7 and 14.1 times higher than those of state-of-the-art commercial Pt/C. The 92.5% of original mass activity can be maintained for porous $Pt_{61}Te_8Rh_{31}$ NRs/C under the corrosive ORR condition, even after 30000 potential cycles of accelerated durability test (ADT). Simultaneously, the selective introduction of Te with self-repairing property and oxophilic Rh favors the electronic structure modification and optimizes the Pt-O binding strength, which endows the porous $Pt_{61}Te_8Rh_{31}$ NRs/C with remarkable self-breathing MEA performance (2.3 times of power density enhancement, only 1.3% cell voltage loss after constant current discharge at 200 mA cm^{-2} for 240 h) in a single self-breathing H_2-air fuel cell medium. More importantly, the MEA with porous $Pt_{61}Te_8Rh_{31}$ NRs/C can readily achieve the highest power densities of 743.4 and 1976.1 mW cm^{-2} at 150 kPa in the H_2/air and H_2/O_2 media, respectively, much higher than those of MEA with commercial Pt/C (555.4 and 1338.8 mW cm^{-2}) under the same test condition. Furthermore, after 30000 cycles of accelerated stress test (AST), the peak power density losses for the MEA with porous $Pt_{61}Te_8Rh_{31}$ NRs/C were measured to be 13.2% and 14.2% at 150 kPa backpressure (BP) in the H_2/air and H_2/O_2 media, respectively, while the MEA with commercial Pt/C displayed 20.1% and 25.7% peak power density losses in the same case. The corresponding density functional theory (DFT) calculations have confirmed that the high electroactivity of porous $Pt_{61}Te_8Rh_{31}$ NRs/C originates from the compensating electronic structures of Pt and Rh sites, which guarantees the fast electron transfer for the ORR process. Meanwhile, the stable protection of Te-5*p* orbitals via the efficient *p-d* coupling effect has contributed to the long-term durability. The corresponding X-ray photoelectron spectroscopy (XPS), X-ray absorption spectroscopy (XAS), and DFT calculation results collectively evidence that the higher fuel cell power density and superior lifetime against commercial Pt/C can be readily realized by the porous $Pt_{61}Te_8Rh_{31}$ NRs/C even under the complicated single fuel cell conditions, demonstrating an efficient Pt-based cathodic nanocatalyst for practical fuel cell catalysis.

Results and Discussions

Preparation and structure of porous $Pt_{61}Te_8Rh_{31}$ NRs/C. The spongy PtTeRh NRs with controlled compositions and PtTe NRs were prepared as the starting nanomaterials via a facile wet-chemical synthesis approach (details in the Experiments section). For the obtained $Pt_3Te_3Rh_2$ NRs, high-angle annular dark-field scanning transmission electron microscopy (HAADF-STEM) and TEM images show that the product has the monodisperse feature with 1D morphology (Fig. S1a-S1c and Fig. S2a). According to the statistic, the average diameter and length of these NRs are 26.9 ± 2.6 nm and 99.0 ± 8.0 nm (Fig. S1d, S1e), respectively, resulting in an aspect ratio of about 3.7. Scanning electron microscopy energy-dispersive X-ray spectroscopy (SEM-EDS) analysis displays that the overall Pt/Te/Rh atomic ratio of these NRs is 36.5/37.2/26.3, very close to the 3/3/2 feeding ratio (Fig. S1f). To further obtain the detailed structural information of $Pt_3Te_3Rh_2$ NRs, powder X-ray diffraction (PXRD), high-resolution TEM (HRTEM), fast Fourier transform (FFT), line-scans, and HAADF-STEM-EDS elemental mappings were collectively performed (Fig. S2b-S2k). PXRD pattern and crystal structure reveal the monoclinic phase of $Pt_3Te_3Rh_2$ NRs with C2/m (12) space group, which is consistent with the standard alloyed phase of PtTe (JCPDS No. 89-6166) (Fig. S2b, S2c). It can be inferred that the introduction of Rh has not changed the crystal phase of PtTe, since the lattice parameters of Rh (JCPDS No. 05-0685) are very close to those of Pt (JCPDS No. 04-0802). Interestingly, the obtained $Pt_3Te_3Rh_2$ NRs have a typical spongy structure with uneven surface/interface and polycrystalline nature, as revealed by the enlarged TEM/HAADF-STEM images, corresponding rainbow-colored TEM/HAADF-STEM images, HRTEM image and related FFT pattern (Fig. S2d-S2g, S2i, S2j and corresponding inset). As shown in Fig. S2e, S2j, the equalized rainbow colors ranging from red (high) to green (low) and blue (high) to yellow (low) obviously display the thickness difference of $Pt_3Te_3Rh_2$ NRs, further demonstrating their spongy nanostructure. The displayed interplanar spacing of $Pt_3Te_3Rh_2$ NRs is 0.28 nm, corresponding to the (111) plane of alloyed $Pt_3Te_3Rh_2$ NRs structure (Fig. S2b, S2f). The white and yellow dotted lines can clearly reveal the presence of uneven surface and partially amorphized area for $Pt_3Te_3Rh_2$ NRs, respectively (Fig. S2f). Moreover, HAADF-STEM images, line-scans, and HAADF-STEM-EDS elemental mappings were jointly used to analyze the distribution of different elements, where Pt, Te, and Rh elements are homogeneously distributed throughout the whole NRs (Fig. S2g-S2i, S2k). Based on all these characterization results, we can conclude the successful construction of spongy $Pt_3Te_3Rh_2$ NRs with uneven surfaces/interfaces and partially amorphized building blocks. Simultaneously, we have also prepared spongy $Pt_3Te_3Rh_1$ NRs, $Pt_3Te_3Rh_3$ NRs, and PtTe NRs with the same phase and similar nanostructures but different compositions only by changing the feeding amount of Te precursor during the synthesis (Figs. S3-S5).

To further optimize the nanostructures of spongy PtTeRh NRs with different compositions and PtTe NRs, a namely called CCEA strategy was applied to produce the corresponding porous

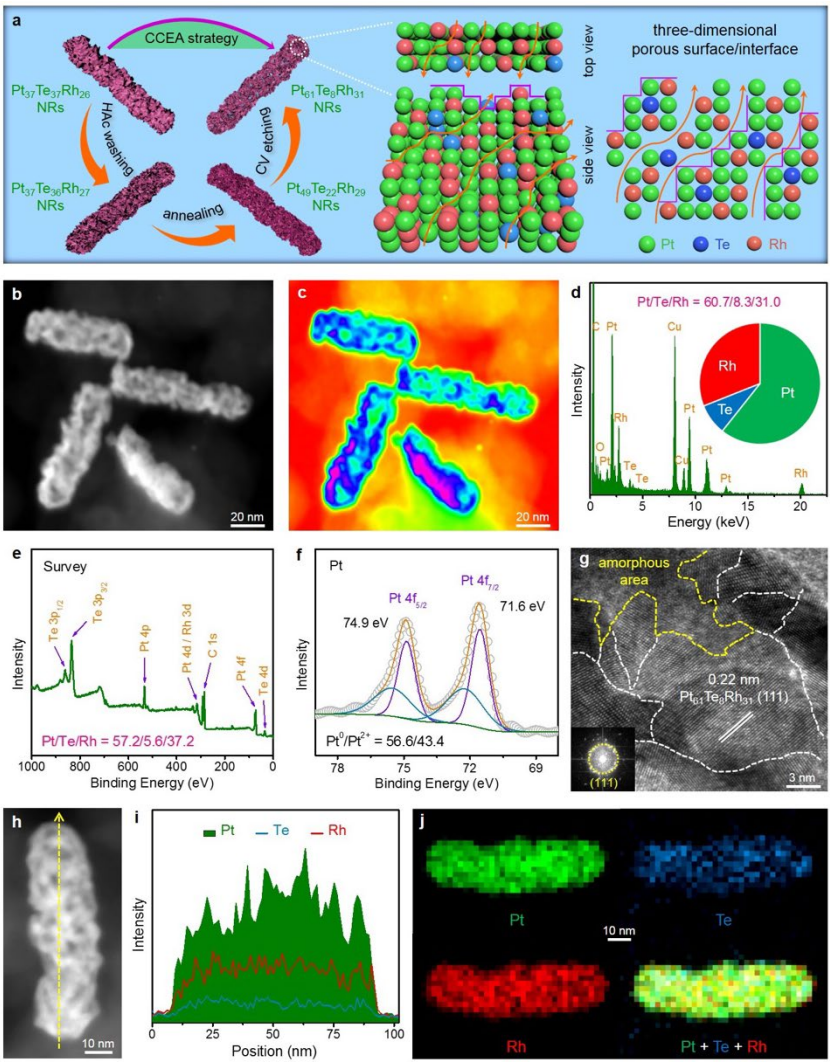

Figure 1 Morphology and structure characterizations of porous $Pt_{61}Te_8Rh_{31}$ NRs/C. (a) Schematic illustration for engineering 3D catalytic surface/interface on spongy $Pt_3Te_3Rh_2$ NRs/C via a controlled CCEA strategy, 3D models and corresponding compositions of $Pt_3Te_3Rh_2$ NRs/C after different CCEA evolution stages, and surface/interface atomic models of porous $Pt_{61}Te_8Rh_{31}$ NRs/C. (b, c) HAADF-STEM image and corresponding rainbow-colored HAADF-STEM image, (d) TEM-EDS, (e) XPS energy survey, (f) Pt 4f XPS spectrum, (g) HRTEM image, (h) HAADF-STEM image, (i) corresponding line-scans, and (j) corresponding HAADF-STEM-EDS elemental mappings of porous $Pt_{61}Te_8Rh_{31}$ NRs/C. The equalized rainbow colors ranging from pink (high) to green (low) in (c) obviously display the thickness difference of porous $Pt_{61}Te_8Rh_{31}$ NRs/C. The inset in (g) is the corresponding FFT pattern. The white and yellow dotted lines in (g) clearly reveal the presence of irregular facet boundaries and amorphous area, respectively.

PtTe-based catalysts, in which the processes of acetic acid (HAc) washing, annealing and cyclic voltammogram (CV) etching are included. The schematic illustration for engineering 3D catalytic surface/interface on spongy $Pt_3Te_3Rh_2$ NRs via the controlled CCEA strategy is shown in the left part of Fig. 1a. In detail, we firstly loaded them on commercial carbon powder (C, Vulcan XC-72R), resulting in the preparation of initial $Pt_3Te_3Rh_2$ NRs/C with no obvious change in morphology and composition (Fig. S6a-S6c). After HAc washing, the nanostructure of $Pt_3Te_3Rh_2$ NRs/C can also be well maintained (Fig. S6d-S6f). After HAc washing and further annealing at 200 °C in air atmosphere for 1 h, however, the overall ratio of Pt/Te/Rh changed from 37.4/36.9/25.7 to 49.0/21.7/29.3, along with a tiny surface structural evolution (Fig. S6g-S6i). The obtained $Pt_{49}Te_{22}Rh_{29}$ NRs/C was then swept in a 0.1 M $HClO_4$ solution for 1000 CV cycles with a scanning rate of 50 mV s^{-1}. After CV etching, $Pt_{61}Te_8Rh_{31}$ NRs/C with nanoporous feature was obtained, as revealed by the results from HAADF-STEM image, rainbow-colored HAADF-STEM image, and TEM-EDS (Fig. 1b-1d). Even after suffering from these complicated treatments, the reconstructed porous $Pt_{61}Te_8Rh_{31}$ NRs with highly open feature can still be highly dispersed on carbon powder (Fig. S7). By XPS, the surface atomic ratio of Pt/Te/Rh was measured to be 57.2/5.6/37.2, which endows the porous $Pt_{61}Te_8Rh_{31}$ NRs/C with a PtRh-rich surface structure (Fig. 1e). As shown in Fig. 1f, the porous $Pt_{61}Te_8Rh_{31}$ NRs/C possesses a high fraction of Pt (II) (43.4%)[27,28], which is in accordance with the uneven surface and porous nature along the 1D longitudinal direction (Fig. 1b, 1c). This conclusion is also reflected by its HRTEM image, in which a large number of irregular facet boundaries (marked by white dotted lines) and partially amorphized area (marked by yellow dotted line) can be clearly observed (Fig. 1g). These irregular facet boundaries and discontinuous lattice fringes can create many step atoms on the surface of porous $Pt_{61}Te_8Rh_{31}$ NRs/C. More importantly, the displayed facet on the surface of porous $Pt_{61}Te_8Rh_{31}$ NRs/C tends to be (111)-dominant, as revealed by

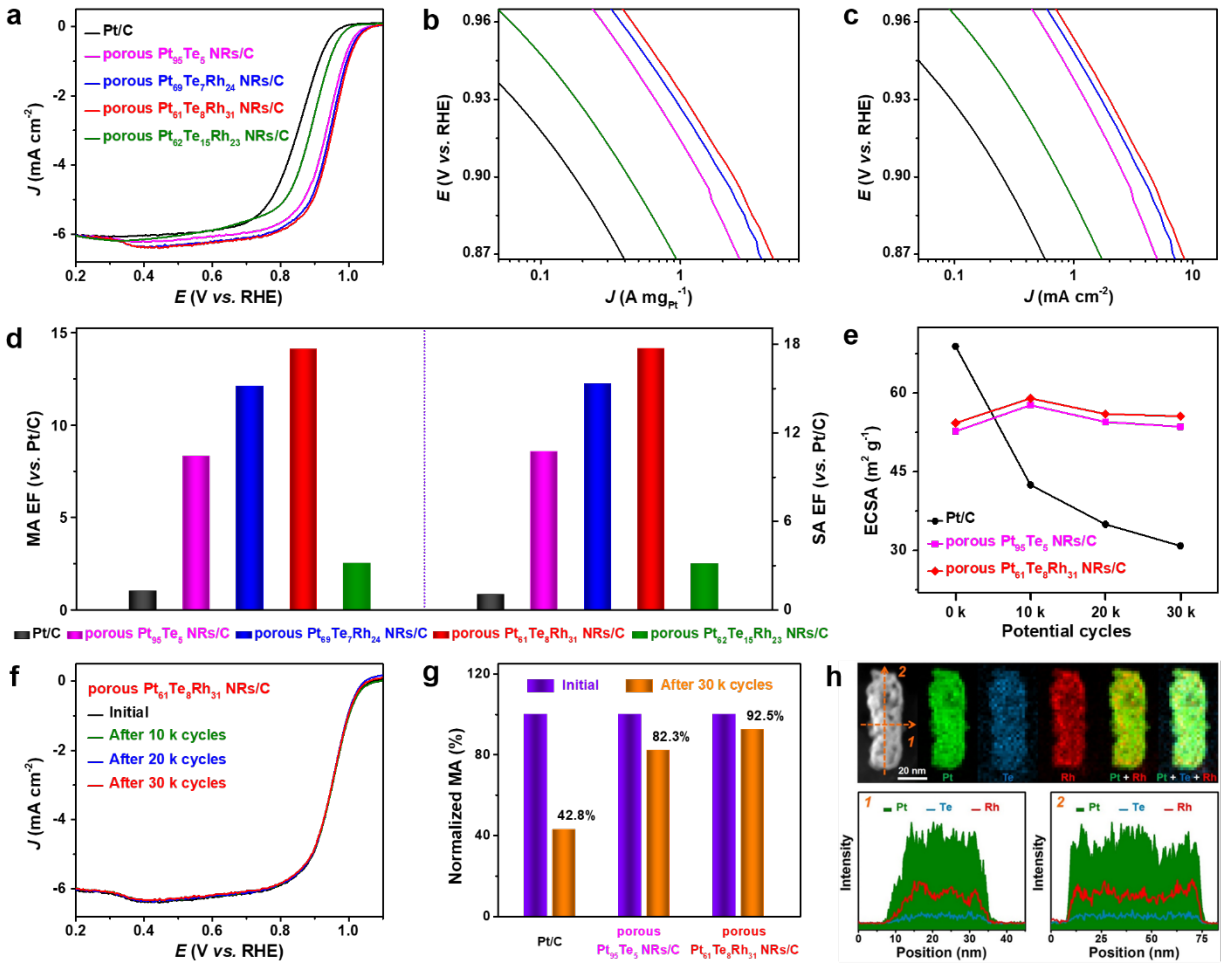

Figure 2 ORR performances of porous $Pt_{61}Te_8Rh_{31}$ NRs/C and its counterparts. (a) Polarization curves of different catalysts. (b, c) MA and SA Tafel plots of different catalysts. (d) MA EF and SA EF of different catalysts in comparison with commercial Pt/C. (e) The ECSA changes of different catalysts before and after different potential cycles between 0.6 and 1.1 V vs. RHE. (f) ORR polarization curves of $Pt_{61}Te_8Rh_{31}$ NRs/C before and after different potential cycles between 0.6 and 1.1 V vs. RHE. (g) The changes on normalized mass activities of different catalysts before and after ADT. (h) HAADF-STEM image, HAADF-STEM-EDS elemental mappings and corresponding line-scans of porous $Pt_{61}Te_8Rh_{31}$ NRs/C after ADT.

its corresponding FFT pattern (inset in Fig. 1g), which may play a significant role in the selective adsorption of key intermediate species[29,30]. In addition, the magnified HAADF-STEM image and corresponding line-scans as well as HAADF-STEM-EDS elemental mappings of an individual $Pt_{61}Te_8Rh_{31}$ NR further demonstrate its 1D porous feature and PtRh-rich surface structure (Fig. 1h-1j). Hence, the porous $Pt_{61}Te_8Rh_{31}$ NRs/C with 3D catalytic surface/interface has been successfully constructed by the CCEA approach. Similarly, porous $Pt_{69}Te_7Rh_{24}$ NRs/C and $Pt_{62}Te_{15}Rh_{23}$ NRs/C originated from spongy $Pt_3Te_3Rh_1$ NRs/C and $Pt_3Te_3Rh_3$ NRs/C can be accordingly obtained, respectively (Fig. S8). Moreover, we have also monitored the successive nanostructure evolutions of PtTe NRs/C during the different CCEA processes, and the porous $Pt_{95}Te_5$ NRs/C can be finally prepared (Fig. S9 and Fig. S10a-S10c).

In particular, the 3D atomic models and corresponding compositions of $Pt_3Te_3Rh_2$ NRs after different CCEA strategy stages were provided to better understand the nanostructure evolutions (left part of Fig. 1a). From the middle and right parts of Fig. 1a, we can see that the surface/interface atomic models display the favorable structure advantage of porous $Pt_{61}Te_8Rh_{31}$ NRs/C for catalysis. Either from the top view or side view, this unique porous nanostructure along the 1D longitudinal direction exhibits many channels at atomic level (denoted by orange lines with arrows), which is beneficial for the efficiency improvement of mass/charge transfer. Furthermore, due to the highly open structure induced by acid etching, a large number of step atoms located on the 3D surfaces or at the irregular facet boundaries have been created, which is beneficial to realize the enhanced catalysis. Considering the synergistic effect arising from the rational combination of different components and anisotropic 1D porous nanostructure, the 3D porous $Pt_{61}Te_8Rh_{31}$ NRs/C is highly expected to exhibit satisfactory ORR performance even in operating fuel cell medium.

ORR performance. To evaluate the electrochemical properties of different porous PtTeRh NRs/C and porous $Pt_{95}Te_5$ NRs/C, we firstly selected the cathodic ORR as the model reaction. As a reference, commercial Pt/C (20 wt.% Pt on Vulcan XC-72R C, Pt NPs with the size of 2 to 5 nm) obtained from Johnson Matthey (JM) Corporation was used as the benchmarked catalyst (Fig. S11a, S11b). The CVs of different catalysts were acquired to calculate their electrochemically active surface areas (ECSAs). The ECSAs were measured to be 54.1, 54.3, 53.5, 52.7, and 68.9 $m^2\ g^{-1}$ for porous $Pt_{62}Te_{15}Rh_{23}$ NRs/C, porous $Pt_{61}Te_8Rh_{31}$ NRs/C,

porous $Pt_{69}Te_7Rh_{24}$ NRs/C, porous $Pt_{95}Te_5$ NRs/C, and commercial Pt/C, respectively (Fig. S12 and Table S1). The ECSAs of porous PtTeRh NRs/C with different compositions are very close to that of porous $Pt_{95}Te_5$ NRs/C due to their similar nanostructures.

The ORR polarization curves of different catalysts were recorded in Fig. 2a. Strikingly, the porous $Pt_{61}Te_8Rh_{31}$ NRs/C displays the most positive half-wave potential, suggesting its highest ORR activity. The mass activity (MA) and specific activity (SA) Tafel plots for different catalysts also demonstrate the highest ORR activity of porous $Pt_{61}Te_8Rh_{31}$ NRs/C (Fig. 2b, 2c). To be specific, the MA of porous $Pt_{61}Te_8Rh_{31}$ NRs/C can reach up to 2.4 A mg^{-1}_{Pt} at 0.90 V vs. RHE, 5.7, 1.2, 1.7, and 14.1 times higher than those of $Pt_{62}Te_{15}Rh_{23}$ NRs/C, $Pt_{69}Te_7Rh_{24}$ NRs/C, $Pt_{95}Te_5$ NRs/C, and Pt/C, respectively, representing the highest ORR mass activity among all the catalysts investigated (Table S1). Simultaneously, the porous $Pt_{61}Te_8Rh_{31}$ NRs/C exhibits the highest SA of 4.4 mA cm^{-2} with 1.6 and 17.7 enhancement factors (EFs) versus $Pt_{95}Te_5$ NRs/C and Pt/C, respectively (Table S1). Compared with the ORR activities of state-of-the-art Pt-based nanocatalysts from recent 5 years-published works, the ORR activity of porous $Pt_{61}Te_8Rh_{31}$ NRs/C is very competitive (Table S2). It should be mentioned that the ORR activities of different porous PtTeRh NRs/C and porous $Pt_{95}Te_5$ NRs/C are much greater than that of Pt/C (Fig. 2d and Table S1), which further reveals that engineering the 3D surface/interface in different spongy PtTeRh NRs and PtTe NRs is an effective approach to boosting oxygen reduction catalysis.

We have also performed the ADT to evaluate the ORR stability of each catalyst. Figure 2e, 2f and Fig. S13 as well as Fig. S14 show the changes of CVs and ORR polarization curves for these five catalysts before and after 10000, 20000, and 30000 potential cycles. Generally, the commonly reported catalysts exhibit gradually decreased ECSAs during the long-term ORR stability tests. However, these kinds of different porous PtTeRh NRs/C and porous $Pt_{95}Te_5$ NRs/C have shown negligible changes in their ECSAs during the ADT process, very different from the case of commercial Pt/C (Fig. 2e, Fig. S13a, S13c, S13e and Fig. S14a, S14c). The porous $Pt_{61}Te_8Rh_{31}$ NRs/C and porous $Pt_{95}Te_5$ NRs/C have maintained 102.4% and 101.7% of their initial ECSAs, respectively, while commercial Pt/C has exhibited 55.2% of ECSA loss after the ADT (Fig. 2e). Furthermore, the MA loss for porous $Pt_{61}Te_8Rh_{31}$ NRs/C is only 7.5%, much less than those of porous $Pt_{95}Te_5$ NRs/C (17.7% loss) and commercial Pt/C (57.2% loss) (Fig. 2f, 2g and Fig. S13b, S13d). The porous $Pt_{61}Te_8Rh_{31}$ NRs/C also exhibits the lowest MA loss in comparison with porous $Pt_{69}Te_7Rh_{24}$ NRs/C (13.2% loss) and $Pt_{62}Te_{15}Rh_{23}$ NRs/C (23.8% loss), demonstrating the outstanding ORR durability (Fig. 2f and Fig. S14b, S14d). In addition, the morphology, composition, and nano/electronic structure of porous $Pt_{61}Te_8Rh_{31}$ NRs/C after 30000 potential cycles were studied in detail. The 1D morphology of this catalyst can be maintained (Fig. S15a, S15b), but the overall Pt/Te/Rh molar ratio was changed to 78.3/7.3/14.4 (Fig. S15c). Simultaneously, HRTEM images, HAADF-STEM image, corresponding line-scans and HAADF-STEM-EDS elemental mappings of spent porous $Pt_{61}Te_8Rh_{31}$ NRs/C clearly reveal the formation of a newly reconstructed 1D porous nanostructure and the presence of irregular facet boundaries and more partially amorphized areas, firmly demonstrating its structure stability in ORR medium (Fig. 2h and Fig. S15e, S15f). After the ADT, the porous $Pt_{61}Te_8Rh_{31}$ NRs/C displayed a certain change on the surface molar ratio of Pt/Te/Rh (Fig. 1e, 1f and Fig. S15g-S15j), which is in accordance with the result of corresponding nanostructure evolution. Although the 1D shape of porous $Pt_{95}Te_5$ NRs/C can be largely maintained after the ADT, it exhibits a significant structure evolution to a stuffed nanostructure, along with an obvious atomic ratio change of Pt/Te from 95.1/4.9 to 97.1/2.9 (Fig. S10d-S10f). By sharp contrast, obvious size change and serious NP aggregation can be observed for commercial Pt/C after the ORR stability test (Fig. S11c, S11d), further indicating the superior durability of porous $Pt_{61}Te_8Rh_{31}$ NRs/C for ORR.

MEA performance evaluation. Based on the above experimental results, a reasonable ORR mechanism on the surface of porous $Pt_{61}Te_8Rh_{31}$ NRs can be accordingly inferred. Due to the integration of multiple structure advantages, the porous $Pt_{61}Te_8Rh_{31}$ surface possesses abundant 3D catalytic channels, which is very beneficial for the mass/electron transfer (Fig. 3a). The O_2 molecule adsorbed by this multicomponent surface (denoted as $*O_2$) may undergo *OOH, *O, and *OH, etc., finally leading to the formation of H_2O. Particularly, due to the distinctive oxophilic feature of Rh, the adsorption efficiency toward *OH species can be largely improved, resulting in fast ORR kinetics and high activity of porous $Pt_{61}Te_8Rh_{31}$ NRs/C (Fig. 3a). However, even if the whole transformation can also be realized on pure Pt surface, the adsorption efficiency toward *OH species is much lower than that on porous $Pt_{61}Te_8Rh_{31}$ surface (Fig. 3b), which is in accordance with our experimental results (Fig. 2). The adsorption energy of *OH species has been regarded as an effective descriptor of ORR performance for Pt-based catalysts[30-32]. Hence, we have realized a remarkable oxygen reduction catalysis via rationally tuning the adsorption energy of *OH species on the surface of porous $Pt_{61}Te_8Rh_{31}$ NRs/C.

Considering the fast ORR kinetics and superior catalytic/structural stability of porous $Pt_{61}Te_8Rh_{31}$ NRs/C, we further evaluated its MEA performance as the cathodic catalyst for PEMFC in both self-breathing and operating fuel cell media. Firstly, the voltage-current (*V-I*) polarization curves and power density distributions of porous $Pt_{61}Te_8Rh_{31}$ NRs/C and commercial Pt/C were measured under the ambient temperature and pressure conditions (Fig. 3c). Obviously, the MEA catalyzed by porous $Pt_{61}Te_8Rh_{31}$ NRs/C exhibits a higher current density throughout the whole polarization curve scan than the case of MEA with commercial Pt/C, suggesting its superior MEA performance, which can be further confirmed by the corresponding power density curves (Fig. 3c, 3d). The MEA with porous $Pt_{61}Te_8Rh_{31}$ NRs/C shows the normalized peak power density of 1023.8 W g^{-1}_{Pt}, which is 2.3 times higher than that of the MEA with commercial Pt/C (446.7 W g^{-1}_{Pt}) (Fig. 3d and Table S3). Notably, it is found that the normalized peak power density of porous $Pt_{61}Te_8Rh_{31}$ NRs/C for self-breathing PEMFC is better than those of the most reported state-of-the-art catalysts (Table S4), showing a great potential in single self-breathing PEMFC. It should be mentioned that the higher power density can be reached at the lower loading amount of Pt for porous $Pt_{61}Te_8Rh_{31}$ NRs/C (Table S3), directly indicating that

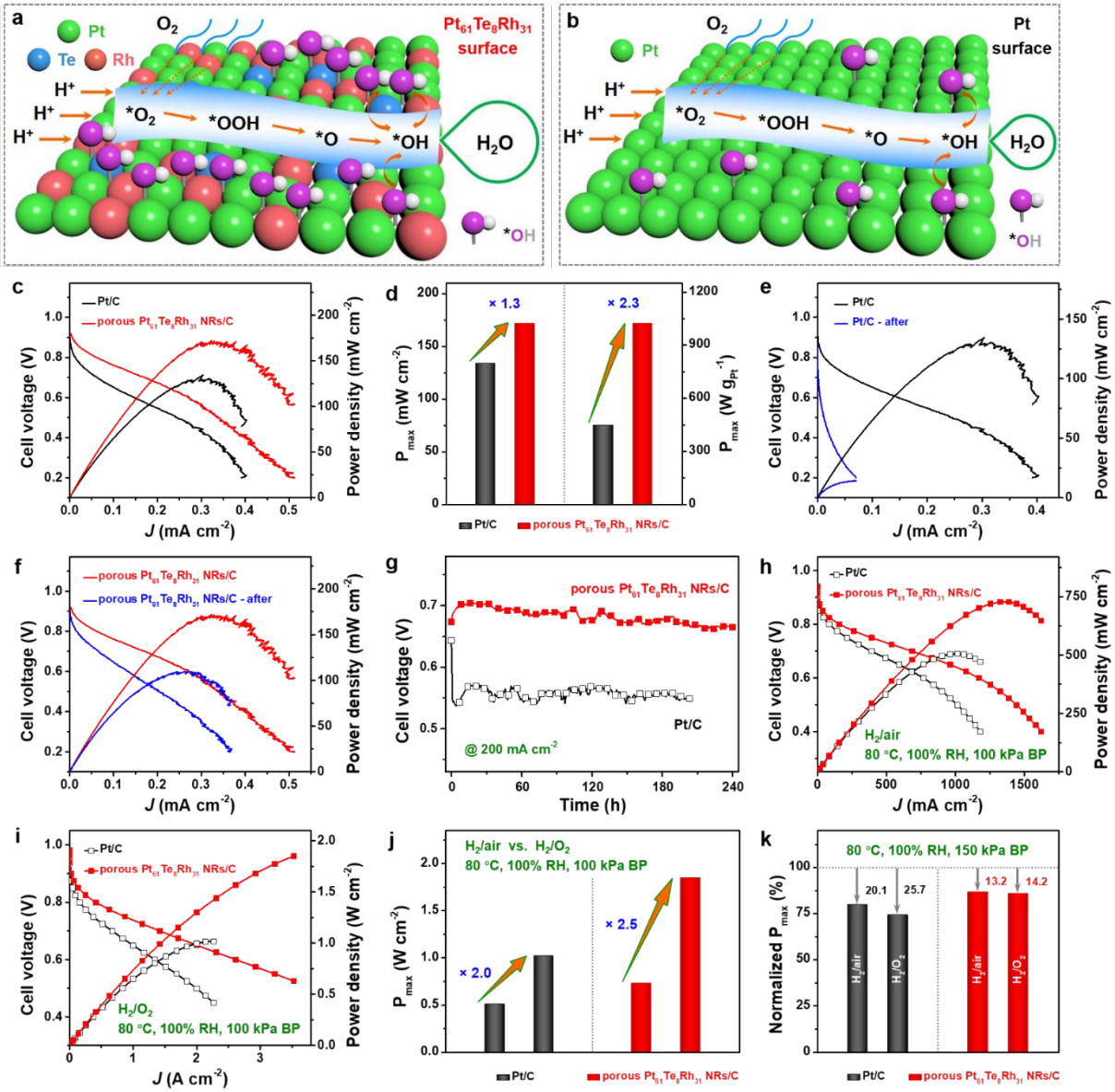

Figure 3 MEA performance evaluation of porous $Pt_{61}Te_8Rh_{31}$ NRs/C in single cell. The adsorption and dynamic transformation process of O_2 on the surfaces of (a) $Pt_{61}Te_8Rh_{31}$ and (b) Pt. (c) Self-breathing fuel cell polarization curves and power density curves of different cathodic catalysts. (d) Histogram of maximum power densities and normalized power densities for different catalysts. (e, f) Polarization curves and power density curves of different catalysts before and after (g) constant current testing at 200 mA cm^{-2} for more than 205 h. PEMFC polarization curves and power density curves of different cathodic catalysts in (h) H_2/air and (i) H_2/O_2 media at 100 kPa BP. (j) Histogram of maximum power densities for different catalysts in H_2/air and H_2/O_2 media at 100 kPa BP. (k) The changes on normalized maximum power densities of different catalysts before and after 30000 cycles at 150 kPa BP.

porous $Pt_{61}Te_8Rh_{31}$ NRs/C is an efficient cathodic catalyst for self-breathing MEA catalysis.

The lifetime test for each catalyst in this MEA medium was also performed. Compared with the initial power density distribution, commercial Pt/C exhibited a large decay of peak power density (89.6%) after the constant current discharge at 200 mA cm^{-2} for 205 h, showing the poor catalytic lifetime performance (Fig. 3e, 3g). However, much better than that of commercial Pt/C, 35.7% decay of peak power density can be achieved for the MEA catalyzed by porous $Pt_{61}Te_8Rh_{31}$ NRs/C (Fig. 3f). Furthermore, after 240 h of constant current discharge at 200 mA cm^{-2}, the voltage showed only 1.3% of loss for the MEA with porous $Pt_{61}Te_8Rh_{31}$ NRs/C (from 0.674 V to 0.665 V, only 9 mV decay), while the MEA with commercial Pt/C exhibited 14.2% of voltage loss after 205 h of constant current discharge (from 0.643 V to 0.552 V, 91 mV decay), clearly displaying the excellent self-breathing MEA lifetime of porous $Pt_{61}Te_8Rh_{31}$ NRs/C (Fig. 3g and Table S2). Hence, it is demonstrated that the porous $Pt_{61}Te_8Rh_{31}$ NRs/C has great potential to be applied as a highly active and durable catalyst for both ORR and self-breathing MEA catalysis.

To further demonstrate the structural advantage of porous $Pt_{61}Te_8Rh_{31}$ NRs/C versus commercial Pt/C, they were also employed as the cathodic catalysts in the MEA of PEMFC under the operating fuel cell conditions. As shown in Fig. 3h, 3i, the MEA with porous $Pt_{61}Te_8Rh_{31}$ NRs/C can always exhibit the higher cell voltage and power density in comparison with commercial Pt/C throughout the whole polarization curve scan

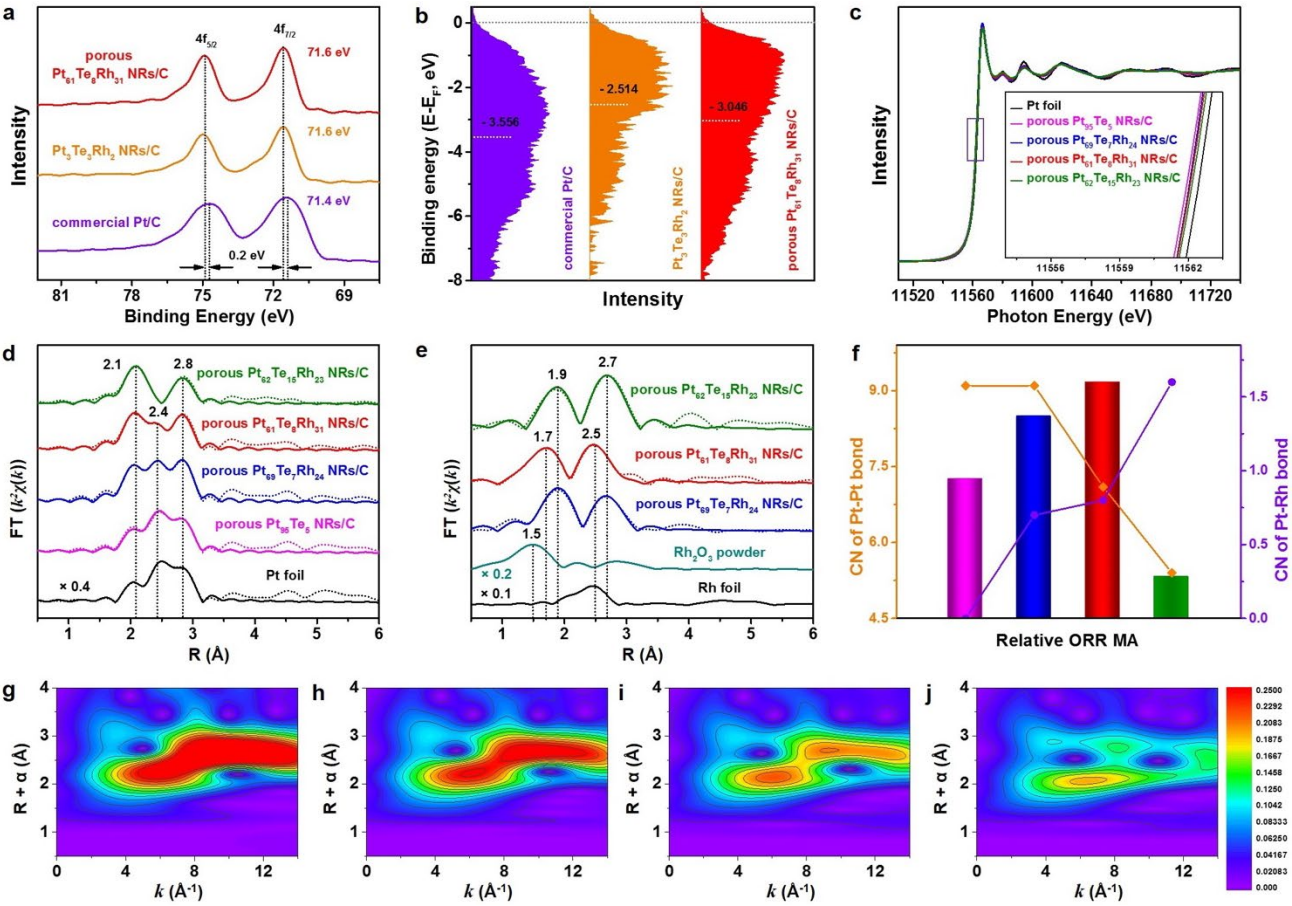

Figure 4 XPS and XAS evidences of performance enhancement catalyzed by porous $Pt_{61}Te_8Rh_{31}$ NRs/C. (a) Pt 4f XPS spectra and (b) surface valence band photoemission spectra of porous $Pt_{61}Te_8Rh_{31}$ NRs/C, $Pt_3Te_3Rh_2$ NRs/C and commercial Pt/C. Pt L_3-edge (c) XANES and (d) EXAFS spectra of different catalysts. The inset in (c) is the magnified near-edge structures of different catalysts. (e) Rh K-edge EXAFS spectra of different catalysts. (f) The direct relationship between CNs of Pt-Pt/Pt-Rh bonds and relative ORR MA for different porous PtTeRh NRs/C catalysts. The magenta, blue, red, and green histograms represent porous $Pt_{95}Te_5$ NRs/C, porous $Pt_{69}Te_7Rh_{24}$ NRs/C, porous $Pt_{61}Te_8Rh_{31}$ NRs/C, and porous $Pt_{62}Te_{15}Rh_{23}$ NRs/C, respectively. Wavelet transform analyses of the Pt L_3-edge EXAFS data for (g) porous $Pt_{95}Te_5$ NRs/C, (h) porous $Pt_{69}Te_7Rh_{24}$ NRs/C, (i) porous $Pt_{61}Te_8Rh_{31}$ NRs/C, and (j) porous $Pt_{62}Te_{15}Rh_{23}$ NRs/C.

at 100 kPa BP in both H_2/air and H_2/O_2 media. The peak power densities for the MEA with porous $Pt_{61}Te_8Rh_{31}$ NRs/C under H_2/air and H_2/O_2 conditions were measured to be 727.8 mW cm^{-2} and 1851.0 mW cm^{-2}, respectively, much higher than those of MEA with commercial Pt/C (505.6 mW cm^{-2} and 1017.5 mW cm^{-2}). It is found that the peak power density for the MEA with porous $Pt_{61}Te_8Rh_{31}$ NRs/C and commercial Pt/C at 100 kPa BP in H_2/O_2 medium is 2.5 times and 2.0 times higher than their respective case in H_2/air medium (Fig. 3j), further demonstrating the superior oxophilic property of porous $Pt_{61}Te_8Rh_{31}$ NRs/C, which is consistent with the results of ORR and self-breathing MEA catalysis. Even under the condition of 150 kPa BP in H_2/air and H_2/O_2 media, we can also obtain the similar conclusion (Fig. S16). In fact, no matter in H_2/air or H_2/O_2 medium, porous $Pt_{61}Te_8Rh_{31}$ NRs/C exhibits the BP-dependent power density, and at 150 kPa BP, the maximum power densities of porous $Pt_{61}Te_8Rh_{31}$ NRs/C can reach up to 743.4 mW cm^{-2} and 1976.1 mW cm^{-2} in H_2/air and H_2/O_2 media, respectively (Fig. S17), much higher than the case of commercial Pt/C (555.4 mW cm^{-2} and 1338.8 mW cm^{-2}) under the same condition (Fig. S16c and Table S5). We found that the power density of porous $Pt_{61}Te_8Rh_{31}$ NRs/C in H_2/O_2 medium is even better than those of the most state-of-the-art Pt-based nanocatalysts from recent 5 years-published works (Table S6), further demonstrating the obvious structural advantage of porous $Pt_{61}Te_8Rh_{31}$ NRs/C. Moreover, we also evaluated the lifetime of MEA for porous $Pt_{61}Te_8Rh_{31}$ NRs/C and commercial Pt/C under the operating fuel cell conditions (Fig. S18a, S18b). During the whole process of 30000 cycles, we can see that the current density loss of porous $Pt_{61}Te_8Rh_{31}$ NRs/C is obviously less than that of commercial Pt/C, revealing the better MEA durability of porous $Pt_{61}Te_8Rh_{31}$ NRs/C (Fig. S18c, S18d). Simultaneously, we also measured the PEMFC polarization curves and power density curves of different catalysts before and after 30000 cycles at 100/150 kPa BP in H_2/air and H_2/O_2 media (Fig. S19). As a result, porous $Pt_{61}Te_8Rh_{31}$ NRs/C exhibits the 13.2% and 14.2% losses in maximum power density at 150 kPa BP in H_2/air and H_2/O_2 media, respectively, much better than those of commercial Pt/C (20.1% and 25.7% losses) (Fig. 3k and Table S5), confirming the superior MEA lifetime of porous $Pt_{61}Te_8Rh_{31}$ NRs/C. Based on the collective results from ORR, MEA catalysis of self-breathing fuel cell and operating fuel cell, we can firmly conclude the fact of obvious structural advantage for porous $Pt_{61}Te_8Rh_{31}$ NRs/C versus commercial Pt/C.

Origin of performance enhancement. To understand the significantly improved ORR kinetics and MEA performance of porous $Pt_{61}Te_8Rh_{31}$ NRs/C in comparison with its counterparts, XPS and XAS were collectively used to investigate the local electronic structures of different catalysts. We found that the

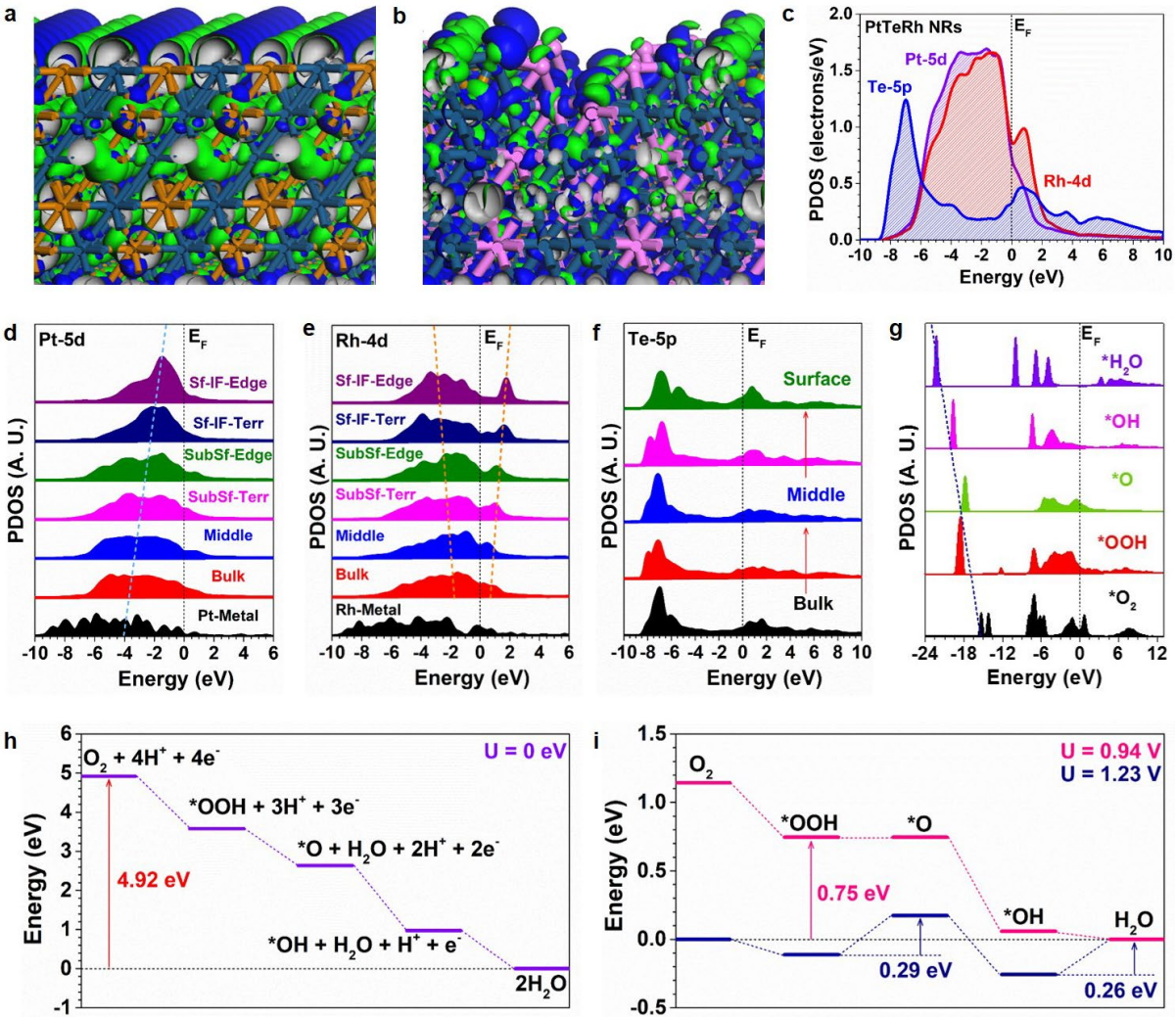

Figure 5 DFT calculations of ORR pathways on PtTeRh surfaces/interfaces. The 3D contour plot of electronic distribution near Fermi level of (a) PtTe NRs and (b) PtTeRh NRs. The green, orange and pink balls represent Pt, Te, and Rh atoms, respectively. The blue and green isosurfaces represent bonding and anti-bonding orbitals, respectively. (c) The PDOS of PtTeRh NRs. (d) The site-dependent PDOS of Pt-5*d* in PtTeRh NRs. (e) The site-dependent PDOS of Rh-4*d* in PtTeRh NRs. (f) The site-dependent PDOS of Te-5*p* in PtTeRh NRs. (g) The PDOS of key ORR adsorbates in PtTeRh NRs. (h) The ORR reaction trend of PtTeRh NRs under U = 0 V. (i) The ORR reaction trend of PtTeRh NRs under U = 0.94 V.

peak positions of Pt $4f_{7/2}$ for porous $Pt_{61}Te_8Rh_{31}$ NRs/C and initial $Pt_3Te_3Rh_2$ NRs/C are both located at 71.6 eV, which is 0.2 eV positive than that of commercial Pt/C (Fig. 4a and Fig. S20). It is demonstrated that the selective introduction of Te and Rh can effectively modify the electronic structure of Pt for porous $Pt_{61}Te_8Rh_{31}$ NRs/C. Simultaneously, the surface valence band photoemission spectra of different catalysts were obtained by XPS. The *d*-band center position of porous $Pt_{61}Te_8Rh_{31}$ NRs/C (-3.046 eV) is 0.53 eV negative than that of initial $Pt_3Te_3Rh_2$ NRs/C (-2.514 eV), but positive than that of commercial Pt/C (Fig. 4b). The suitable *d*-band center position contributes to the highest ORR and MEA performances of porous $Pt_{61}Te_8Rh_{31}$ NRs/C. Furthermore, the high fraction of Pt (II) in porous $Pt_{61}Te_8Rh_{31}$ NRs/C (43.4%, Fig. 1f) is ascribed to the presence of strong surface boundary effect and abundant defects (Fig. 1g), which is beneficial for the enhanced ORR kinetics. Even after the long-term ADT for ORR, the porous $Pt_{61}Te_8Rh_{31}$ NRs/C can still display the high fraction of Pt (II) on the surface (41.4%, Fig. S15h), further demonstrating its durable active center, favorable nanostructure and electronic configuration, which is in accordance with the electrocatalytic results.

X-ray absorption near-edge structure (XANES) and extended X-ray absorption fine structure (EXAFS) measurements were performed to further analyze the local electronic structures of different catalysts. Unusually, the Pt L_3-edge XANES spectra reveal that the valence of Pt in various PtTe- and PtTeRh-based NRs/C is neither similar to that of the referenced Pt foil (metallic state), nor similar to that of PtO_2 (oxidized state), which can be ascribed to the unconventional compositions of PtTe and PtTeRh (Fig. 4c and Fig. S21a). From the enlarged near-edge structures, we found that the Pt in different porous PtTeRh NRs/C exhibit a more negative valence than Pt foil, revealing the more active electronegativity and reactivity for ORR (inset in Fig. 4c)[30]. Simultaneously, we analyzed the Pt L_3-edge EXAFS spectra of different catalysts in detail (Fig. 4d and Fig. S21b). To be specific, Pt foil shows the typical radial distance (R value) of Pt-Pt bond (~2.76 Å). As for the spongy PtTe NRs/C and porous $Pt_{95}Te_5$ NRs/C, their Pt L_3-edge EXAFS spectra display three obvious R values of ~2.1 Å, ~2.5 Å, and ~2.8 Å, which can correspond to the Pt-O, Pt-M (M = Te or Rh), and Pt-Pt bonds, respectively. Compared with the spongy PtTe NRs/C, the porous

$Pt_{95}Te_5$ NRs/C exhibits a much lower R value at ~2.5 Å and higher R value at ~2.8 Å due to the large loss of Te. Similarly, different porous PtTeRh NRs/C also show different peak intensities for Pt-O, Pt-M (M = Te or Rh), and Pt-Pt bonds in comparison with the corresponding PtTeRh NRs/C with different compositions. Due to the introduction of Te and Rh atoms with controlled amounts, we found that the R values of porous $Pt_{95}Te_5$ NRs/C, porous $Pt_{69}Te_7Rh_{24}$ NRs/C, porous $Pt_{61}Te_8Rh_{31}$ NRs/C, and porous $Pt_{62}Te_{15}Rh_{23}$ NRs/C reduced from 2.76 Å (R value from Pt foil) to 2.75, 2.75, 2.73, and 2.72 Å, respectively. Obviously, from porous $Pt_{95}Te_5$ NRs/C to porous $Pt_{62}Te_{15}Rh_{23}$ NRs/C, the peak intensity of Pt-M bond shows a gradually decreasing tendency. Particularly, the regulated small quantity of Pt-M bond in porous $Pt_{61}Te_8Rh_{31}$ NRs/C induces that the intensities of peaks at ~2.1 Å and at ~2.8 Å are nearly equal, that is, the Pt-O bond strength located in porous $Pt_{61}Te_8Rh_{31}$ NRs/C is very close to that of Pt-Pt bond. Along with the above electrochemical result, it is demonstrated that roughly equal proportions of Pt-O bond and Pt-Pt bond endow the porous $Pt_{61}Te_8Rh_{31}$ NRs/C with highest ORR/MEA performances. More importantly, the coordination number (CN) of Pt-Pt bond for porous $Pt_{61}Te_8Rh_{31}$ NRs/C was fitted to be about 7.1, lower than those of porous $Pt_{95}Te_5$ NRs/C and porous $Pt_{69}Te_7Rh_{24}$ NRs/C, but higher than that of porous $Pt_{62}Te_{15}Rh_{23}$ NRs/C (Table S7), which is in accordance with the case of ORR activity for these four catalysts. Hence, the optimized bond ratio of Pt-O/Pt-Pt (relative binding strength of Pt-O and Pt-Pt) and suitable (relatively low) Pt-Pt CN can be ascribed to the unique 1D porous feature of $Pt_{61}Te_8Rh_{31}$ NRs/C.

We also further analyzed the local electronic structures of different catalysts based on the Rh K-edge XAS spectra. From the Rh K-edge EXAFS spectra of Rh foil and Rh_2O_3 powder, we can clearly observe the presence of two peaks at ~1.5 Å (R value from Rh_2O_3 powder) and ~2.5 Å (R value from Rh foil), which can be assigned to the Rh-O coordination and Rh-Rh coordination, respectively (Fig. 4e). Different from the cases in Rh foil, Rh_2O_3 powder, $Pt_3Te_3Rh_1$ NRs/C, and $Pt_3Te_3Rh_3$ NRs/C, $Pt_3Te_3Rh_2$ NRs/C exhibits two peaks at ~1.7 Å and ~2.5 Å due to its unique composition (Fig. S22). Even after etching, the porous $Pt_{61}Te_8Rh_{31}$ NRs/C can still keep its initial bond positions (Fig. 4e and Fig. S22), revealing its bond stability. Moreover, we have also summarized the fitting parameters of Rh K-edge EXAFS spectra in Table S8, where the CN of Rh-Te bond for porous $Pt_{61}Te_8Rh_{31}$ NRs/C was fitted to be 9.3, which is the highest one among all the catalysts investigated. Simultaneously, porous $Pt_{61}Te_8Rh_{31}$ NRs/C displays the lowest Rh-Pt bond CN of 3.5, being consistent with its optimized nano/electronic structure and highest ORR/MEA performances. Based on these above analyses, we can logically infer the direct relationship between CNs of Pt-Pt/Pt-Rh bonds and relative ORR MA for different porous PtTeRh NRs/C (Fig. 4f), in which the porous $Pt_{61}Te_8Rh_{31}$ NRs/C with moderate CNs of Pt-Pt and Pt-Rh bonds is provided with the highest cathodic catalytic performances for PEMFC. Furthermore, we also performed the wavelet transform (WT) analyses to confirm the Pt-Pt/Pt-Rh bond differences for Pt foil, PtO_2, PtTeRh NRs/C with different compositions, porous $Pt_{95}Te_5$ NRs/C, and different porous PtTeRh NRs/C (Fig. 4g-4j and Fig. S23). As a result, the WT analysis of porous $Pt_{61}Te_8Rh_{31}$ NRs/C reveals two maxima at about 6.1 and 9.3 $Å^{-1}$, which can be assigned to the Pt-O and Pt-Pt coordinations, respectively. By contrast, no matter from the WT analyses of Pt L_3-edge EXAFS data or from the Rh K-edge EXAFS data (Fig. 4g-4j, Fig. S23 and Fig. S24), we can clearly distinguish the unprecedented coordination center of porous $Pt_{61}Te_8Rh_{31}$ NRs/C, which results from its optimized nanostructure and unique local electronic structure modified by the suitable amounts of Te and Rh atoms.

Mechanism investigation. To further shed light on the origins of remarkable ORR and MEA performances of porous $Pt_{61}Te_8Rh_{31}$ NRs/C, we interpret the improved catalytic mechanism from the perspectives of electronic structures and energetic reaction trends by DFT calculations. We have compared the electronic distributions near the Fermi level (E_F) of both PtTe and PtTeRh NRs (Fig. 5a, 5b). PtTe has displayed highly ordered orbital distributions, in which the Pt and Te sites dominate the bonding and anti-bonding orbitals, respectively. In comparison, owing to the abundant interface regions, the PtTeRh NRs surface is highly uneven with many terraces and edges existing in the material, which are consistent with the experiments. Among the low-coordinated regions near the interface, Pt sites at the edge and terrace show the main contributions to the bonding orbitals, which play as the active sites for the ORR process. Meanwhile, the projected partial density of states (PDOS) have revealed the electronic contributions (Fig. 5c). Notably, the Pt-5*d* orbitals show the occupation near the E_F, which supports the efficient electron transfer efficiency. Rh-4*d* orbitals exhibit a good overlapping with Pt-5*d* orbitals, indicating the tight bonding of PtTeRh to guarantee the long-term stability of ORR performances. Te-5*p* orbitals not only show the deep position as the electron reservoir but also cover both Pt-5*d* and Rh-4*d* orbitals, resulting in the efficient *p-d* coupling effect. This guarantees the stable valence state of both Pt and Rh during ORR. With such an electronic environment, both high electroactivity and long-term stability are guaranteed. To obtain the promotion effect of the abundant interfaces, the site-dependent PDOSs are displayed (Fig. 5d). Compared to the Pt metal, Pt-5*d* orbitals in PtTeRh demonstrate a much closer distance to E_F. From the bulk to the surface, we notice the gradual upshifting of the *d*-band center, supporting an improved electroactivity. More importantly, the existence of terrace and edge on catalyst surface has further reflected a sharp peak of Pt-5*d* orbitals, leading to a more efficient electron transfer of active sites. Notably, we notice an opposite redox trend of Rh-4*d* orbitals (Fig. 5e). From the bulk to the surface, the Rh-4*d* orbitals have demonstrated enlarging e_g-t_{2g} splitting trend, leading to the decreasing valence states. Such a compensating PDOS trend with Pt-5*d* orbitals guarantees the high electroactivity of the structure. Moreover, compared to the metallic Rh, Rh sites display higher valence states. Meanwhile, Te is also playing a significant role in high electroactivity (Fig. 5f). We have observed highly stable Te-5*p* orbitals from the bulk to the surface, which enables the efficient electron exchange via the robust *p-d* coupling within the PtTeRh NRs. Moreover, Te-5*p* orbitals also well protect the electroactive Pt and Rh sites during the long-term ORR process with stable electronic structures. With the synergistic effect by Pt, Rh, and Te sites, the efficient electron transfer during ORR is achieved (Fig. 5g). The PDOS of key intermediates of ORR has shown a highly linear correlation for the σ orbitals of O-species, which determines the high efficiency of intermediate conversions. From the initial O_2 to the final product H_2O, the downshifting trend reveals the efficient reduction process.

The energetic trend is also revealed to demonstrate the energetic trend of PtTeRh NRs (Fig. 5h). From the initial adsorption of O_2, the continuous downhill trend is observed for the ORR process under the short-cut circuit of the cell (U = 0 V). The smallest energy drop is noted for the conversion of [*OOH + $3H^+$ + $3e^-$] → [*O + H_2O + $2H^+$ + $2e^-$]. When applying the equilibrium potential of 1.23 V, the largest energy barrier of 0.29 eV has been noticed for the conversion from *OOH to O* (Fig. 5i). The corresponding onset potential has been calculated to be 0.94 V, which should be the highest potential for all the reaction steps to be exothermic. With U = 0.94 V, we notice the equal energy cost for the reaction step of [*OOH + $3H^+$ + $3e^-$] and [*O + H_2O + $2H^+$ + $2e^-$], where all the reaction steps still display the downhill trend to guarantee the efficient ORR process. Accordingly, both electronic structures and reaction energies have confirmed the high electroactivity of PtTeRh NRs for the ORR process.

Conclusions

In this work, we have successfully realized the directed engineering of unique 3D surfaces/interfaces in spongy PtTeRh NRs with different compositions to create a novel class of multicomponent Pt-based PNMs via a controlled CCEA strategy for the first time. Integrating multiple advantages of optimized tricomponent synergistic effect, 3D PtRh-rich surface/interface, and favorable electronic configuration, the optimized porous $Pt_{61}Te_8Rh_{31}$ NRs/C exhibits the highest mass and specific activities for ORR among all the catalysts investigated, in which the corresponding EFs can reach up to 14.1 and 17.7 in comparison with commercial Pt/C. Even after 30000 potential cycles of ADT, only 7.5% MA loss has been found under the strong acidic condition, indicating its outstanding ORR stability. Furthermore, the porous $Pt_{61}Te_8Rh_{31}$ NRs/C exhibits the striking power density of 1023.8 W g^{-1}_{Pt} and negligible voltage loss of only 1.3% during the long-term lifetime test (240 h constant current discharge at 200 mA cm^{-2}) in a single self-breathing H_2-air fuel cell, much better than those of commercial Pt/C. More importantly, even under harsh operating fuel cell conditions, the porous $Pt_{61}Te_8Rh_{31}$ NRs/C can readily achieve the much higher power density (1976.1 mW cm^{-2}) and longer lifetime (14.2% power density loss after the AST for 30000 cycles) than commercial Pt/C (1338.8 mW cm^{-2} and 25.7% power density loss after the AST for 30000 cycles) at 150 kPa BP in H_2/O_2 medium, demonstrating its great potential to be applied as an efficient cathodic catalyst for PEMFC. The detailed XPS, XAS, and DFT calculations further evidence that the uneven surface and rich interfacial regions in porous $Pt_{61}Te_8Rh_{31}$ NRs/C supply abundant active sites to promote the ORR performance. Pt-5*d* and Rh-4*d* orbitals have shown the opposite evolution trend in electronic structures, which is the key for highly efficient electron transfer, while Te-5*p* orbitals well preserve the robust electroactivity during the long-term ORR process. This study on engineering the 3D surface/interface of porous $Pt_{61}Te_8Rh_{31}$ NRs/C for remarkable ORR and MEA catalysis has provided significant inspiration for the design of advanced cathodic catalysts for practical fuel cell devices and beyond.

Experiments

Materials preparation

Preparation of spongy PtTeRh NRs with different compositions and PtTe NRs

In a typical preparation of spongy $Pt_3Te_3Rh_3$ NRs, tetraammineplatinum (II) nitrate ($Pt(NH_3)_4(NO_3)_2$, 10 mg), potassium tellurite (K_2TeO_3, 6.4 mg), rhodium (III) acetylacetonate ($Rh(acac)_3$, 10.2 mg), L-ascorbic acid (AA, $C_6H_8O_6$, 35.6 mg), polyvinylpyrrolidone (PVP, $MW_{average}$ = 58000, 100 mg), water (5 mL) and ethylene glycol (EG, $C_2H_6O_2$, 5 mL) were added into a vial. After the vial had been capped, the mixture was ultrasonicated for around 1 h. The resulting mixture was transferred to a Teflon-lined stainless-steel autoclave and then heated at 200 °C for 5 h in an oven, before it was cooled to room temperature. The resulting products were collected by centrifugation and washed with an ethanol/acetone (v/v = 1/9) mixture. The synthetic conditions for $Pt_3Te_3Rh_2$ NRs, $Pt_3Te_3Rh_1$ NRs and PtTe NRs are similar to those of PtTeRh NRs except changing the feeding amount of $Rh(acac)_3$ to 6.8 mg, 3.4 mg and 0 mg, respectively.

Characterization

The morphology and size of the NCs were determined by TEM (Hitachi, HT7700) at 120 kV. TEM, HRTEM, FFT, HAADF-STEM, and HAADF-STEM-EDS were conducted on a FEI Tecnai F20 TEM at an accelerating voltage of 200 kV. The samples were prepared by dropping their cyclohexane or ethanol dispersion onto the carbon-coated copper TEM grids using pipettes and dried under ambient condition. PXRD patterns were collected using an X`Pert-Pro X-ray powder diffractometer equipped with a Cu radiation source (λ = 0.15406 nm). Low-resolution EDS was performed on a scanning electron microscope (SEM-EDS, Hitachi, S-4700). All the XPS spectra of different catalysts were collected by XPS (Thermo Scientific, ESCALAB 250 XI). The concentration of all the catalysts was determined by the inductively coupled plasma atomic emission spectroscopy (ICP-AES, 710-ES, Varian). The XAS data were collected at the TPS-44A beamline of the National Synchrotron Radiation Research Center (NSRRC, Hsinchu, Taiwan) using a Si (111) quick-scanning monochromator. All the XAS data were processed according to standard procedures using the Demeter program package (Version 0.9.24).

Electrochemical measurements

The final catalysts were redispersed in a mixture solvent containing isopropanol and Nafion perfluorinated resin solution (5 wt% in lower aliphatic alcohols and water) (v/v = 1/0.005) to form a homogeneous catalyst ink by sonicating for 30 min. Similarly, the commercial Pt/C ink was also prepared. The concentration of Pt of all electrocatalysts was fixed to be 0.4 mg_{Pt} mL^{-1} based on ICP-AES measurement. 5 μL dispersion was transferred onto the glassy-carbon electrode with the loading amount of Pt at 2 μg.

The electrochemical measurements for ORR were performed using a glassy-carbon Rotating Disk Electrode (RDE, Pine Research Instrumentation, diameter: 5 mm, area: 0.196 cm^2)

connected to an installation of rotating electrode speed control (Pine Research Instrumentation, model: AFMSRCE). A leak-free saturated calomel electrode (SCE) after calibration and conversion to RHE was used as the reference electrode and a Pt wire was used as the counter electrode. The electrolyte was 0.1 M $HClO_4$. The loading amount of Pt for all the electrocatalysts was all kept at 10.2 μg_{Pt} cm^{-2}. The CVs were performed at room temperature in N_2-saturated 0.1 M $HClO_4$ solution with the sweep rate of 50 mV s^{-1} and the potential range from -0.25 V to 0.96 V vs. SCE. The ECSA was determined by integrating the hydrogen adsorption charge on the CVs at the rate of 50 mV s^{-1} at room temperature in N_2-saturated 0.1 M $HClO_4$ solution. The process of testing the ORR polarization curves with Ohmic correction is as follows. Firstly, the Ohmic values of working electrodes with tested electrocatalysts were measured with the help of CHI660E electrochemical analyzer (CHI Instrumentation). These values will be used as the testing parameters set in the software of Pine Research Instrumentation. The ORR polarization curve of each electrocatalyst was then measured based on the corresponding Ohmic drop correction. ORR measurements were conducted in 0.1 M $HClO_4$ solutions purged with the saturated O_2 during the measurements. The scan and rotation rates for ORR measurements were 10 mV s^{-1} and 1600 rpm, respectively. In the ORR polarization curves, the current densities were normalized in reference to the geometric area of the glassy carbon electrode (0.196 cm^2). The Koutecky-Levich equation was used to determine the kinetic currents from polarization curves by considering the mass-transport correction. For each catalyst, the kinetic current was normalized to the loading amount of Pt and ECSA in order to generate mass and specific activities, respectively. ADTs were performed at room temperature in 0.1 M $HClO_4$ solutions under a N_2 atmosphere by applying the cyclic potential sweeps between 0.6 and 1.1 V vs. RHE at a sweep rate of 100 mV s^{-1} for 30000 cycles.

Preparation of MEA for practical fuel cell catalysis

The self-breathing MEA with an active area of 1 cm^2 was prepared and used in this study as follows. The catalyst layer was spread on the composite electrode by screen printing. The catalyst ink was prepared by dropping Nafion perfluorinated resin solution into mixed solution of deionized water and isopropanol (v/v = 1/1), and with 11.2% $Pt_{61}Te_8Rh_{31}$ NRs/C or 20% Pt/C catalyst in an ultrasonic bath for 30 min. The Nafion content is 40% in the 20% Pt/C ink. A series of $Pt_{61}Te_8Rh_{31}$ NRs/C inks with different Nafion contents were prepared to discover the optimal content of Nafion. The optimized content of Nafion is 40% in the 11.2% $Pt_{61}Te_8Rh_{31}$ NRs/C ink. The cathodic catalyst loading was 0.30 mg_{Pt} cm^{-2} for self-breathing MEA with Pt/C and 0.17 mg_{Pt} cm^{-2} for self-breathing MEA with $Pt_{61}Te_8Rh_{31}$ NRs/C, while the Pt loading was 0.50 mg_{Pt} cm^{-2} for anode (70% Pt/C, 20% Nafion). After coating the catalyst to the electrode, the electrode is placed at 105 °C for 2 h. The carbon paper (190 μm, Toray) was used as the electrode. The Nafion 212 membrane (50 μm, Dupont) was hot-pressed with two electrodes at a pressure of 4 MPa and a temperature of 130 °C for 2 min.

The electrochemical performance of self-breathing MEA was measured by an electrochemical workstation (CS). The test mode is linear sweep voltammetry, the sweep rate is 2 mV s^{-1} and the cut-off voltage is 0.2 V. During the test, the cathode of self-breathing fuel cell is used as the working electrode, and the anode is used as the counter electrode and reference electrode. The test temperature of self-breathing fuel cell is 25 °C. Specifically, one side of the anode is actively supplied with hydrogen, the other side of the cathode is directly exposed in the air, and the air is passively supplied. The experiments were performed with pure hydrogen at room temperature and atmospheric pressure. The pure hydrogen is prepared from a hydrogen generator. The flow rate of hydrogen is 10 mL min^{-1}. The polarization curve of fuel cell is measured by linear scanning at the rate of 2 mV s^{-1}. The self-breathing fuel cell lifetime test is set to constant current discharge at 200 mA cm^{-2} for at least 205 h.

The MEA with an active area of 25 cm^2 for operating H_2-air/O_2 PEMFC was prepared as follows. The cathodic catalyst ink was prepared by ultrasonic dispersion of catalyst (22.3 mg 11.2% $Pt_{61}Te_8Rh_{31}$ NRs/C or 12.5 mg 20% commercial Pt/C) and 5 wt% Nafion solution in deionized water and isopropanol (v/v = 1/1) mixture for 1 h. The Pt loading of cathodic $Pt_{61}Te_8Rh_{31}$ NRs/C and commercial Pt/C catalysts was 0.10 mg_{Pt} cm^{-2}. The anode catalyst was 20% Pt/C, and the loading was also 0.10 mg_{Pt} cm^{-2}. The MEA was prepared by assembling in order with gasket, carbon paper (190 μm, Toray), anodic catalyst, PEM (12 μm, Gore), cathodic catalyst, carbon paper, and gasket. The effective area of MEA for operating H_2-air/O_2 PEMFC was 5 × 5 cm^2. The catalyst-based MEA for operating H_2-air/O_2 PEMFC was tested at 80 °C with 100% relative humidity (RH) using the 850g fuel-cell test system equipped with 885 potentiostat (100 W, Scribner Associates Inc.). The total outlet BP was adjusted from 50 kPa to 150 kPa with the certain flow rate of H_2 or O_2 (500/1500 mL min^{-1} for anode/cathode in H_2/air medium, 1000/1000 mL min^{-1} for anode/cathode in H_2/O_2 medium). Before the polarization curves were recorded, the MEA was fully activated by holding at 0.85 V, 0.6 V, 0.5 V, and 0.4 V for 1 min, 5 min, 5 min, and 5 min for 5 cycles to stabilize the potential and current density. The AST consisted of potential cycling by square wave between 0.6 and 0.95 V at 3 s at each potential for 30000 cycles. This AST was run at 200/200 mL min^{-1} H_2/N_2, 80/80 °C, 100/100% RH and 100/100 kPa BP in the order of anode/cathode.

DFT calculations

To study the formation and electrochemical performance of PtTeRh NRs, we have applied the DFT calculations within CASTEP packages to reveal both the electronic structures and reaction trend[33]. We have selected the generalized gradient approximation (GGA) and Perdew-Burke-Ernzerhof (PBE) to describe the exchange-correlation interactions[34-36]. Meanwhile, we have set the plane-wave basis cutoff energy to be 380 eV and the ultrasoft pseudopotentials are selected for all the geometry optimizations. The Broyden-Fletcher-Goldfarb-Shannon (BFGS) algorithm has been applied in this work, and

the *k*-points have been applied with coarse quality based on the convergence tests[37]. The PtTeRh NRs have been cleaved from the Pt (111) surfaces with the introduction of Rh and Te atoms. The PtTeRh are PtRh rich on the surface, while Te atoms are mostly distributed from subsurface to bulk. Meanwhile, we have constructed the uneven surfaces based on the experimental characterizations. We have introduced 20 Å vacuum space in the z-axis to allow full relaxations. For all the geometry optimizations, we have set the following convergence criteria: the Hellmann-Feynman forces should not exceed 0.001 eV $Å^{-1}$, and the total energy difference and the inter-ionic displacement should be less than 5×10^{-5} eV $atom^{-1}$ and 0.005 Å, respectively.

Author Contributions

X. Huang and L. Bu conceived and supervised the research. X. Huang and L. Bu designed the experiments. X. Huang, L. Bu, C. Zhan, L. Li, Y. Zhu. and Q. Shao participated in the experimental data analyses and discussions. F. Ning and X. Zhou measured the self-breathing MEA performances of different catalysts. M. Sun and B. Huang performed the DFT simulations. Z. Hu and J. Zhou helped the collection and analysis of XAS data. X. Huang and L. Bu wrote the paper. All authors discussed the results and commented on the manuscript.

Conflicts of interest

There are no conflicts to declare.

Acknowledgements

This work was financially supported by the National Key R&D Program of China (2020YFB1505802; 2021YFA1501101), the Ministry of Science and Technology of China (2017YFA0208200, 2016YFA0204100), the National Natural Science Foundation of China (22025108, U21A20327, 22121001, 21571135), the project of scientific and technologic infrastructure of Suzhou (SZS201708), the Priority Academic Program Development of Jiangsu Higher Education Institutions (PAPD), the Natural Science Foundation of China/RGC Joint Research Scheme (N_PolyU502/21), and the funding for Projects of Strategic Importance of The Hong Kong Polytechnic University (Project Code: 1-ZE2V), and the start-up supports from Xiamen University.

References

1 Y. H. He, S. W. Liu, C. Priest, Q. R. Shi, G. Wu, *Chem. Soc. Rev.* **2020**, *49*, 3484.
2 M. H. Shao, Q. W. Chang, J. P. Dodelet, R. Chenitz, *Chem. Rev.* **2016**, *116*, 3594.
3 M. K. Debe, *Nature* **2012**, *486*, 43.
4 V. R. Stamenkovic, B. Fowler, B. S. Mun, G. F. Wang, P. N. Ross, C. A. Lucas, N. M. Marković, *Science* **2007**, *315*, 493.
5 Y. J. Wang, N. N. Zhao, B. Z. Fang, H. Li, X. T. T. Bi, H. J. Wang, *Chem. Rev.* **2015**, *115*, 3433.
6 M. L. Liu, Z. P. Zhao, X. F. Duan, Y. Huang, *Adv. Mater.* **2019**, *31*, 1802234.
7 L. Z. Bu, N. Zhang, S. J. Guo, X. Zhang, J. Li, J. L. Yao, T. Wu, G. Lu, J. Y. Ma, D. Su, X. Q. Huang, *Science* **2016**, *354*, 1410.
8 M. F. Li, Z. P. Zhao, T. Cheng, A. Fortunelli, C. Y. Chen, R. Yu, Q. H. Zhang, L. Gu, B. V. Merinov, Z. Y. Lin, E. B. Zhu, T. Yu, Q. Y. Jia, J. H. Guo, L. Zhang, W. A. Goddard III, Y. Huang, X. F. Duan, *Science* **2016**, *354*, 1414.
9 L. N. Chong, J. G. Wen, J. Kubal, F. G. Sen, J. X. Zou, J. Greeley, M. Chan, H. Barkholtz, W. J. Ding, D. J. Liu, *Science* **2018**, *362*, 1276.
10 Z. P. Wu, D. T. Caracciolo, Y. Maswadeh, J. G. Wen, Z. J. Kong, S. Y. Shan, J. A. Vargas, S. Yan, E. Hopkins, K. Park, A. Sharma, Y. Ren, V. Petkov, L. C. Wang, C. J. Zhong, *Nat. Commun.* **2021**, *12*, 859.
11 S. Zaman, L. Huang, A. I. Douka, H. Yang, B. You, B. Y. Xia, *Angew. Chem. Int. Ed.* **2021**, *60*, 17832.
12 I. E. L. Stephens, J. Rossmeisl, I. Chorkendorff, *Science* **2016**, *354*, 1378.
13 K. Kodama, T. Nagai, A. Kuwaki, R. Jinnouchi, Y. Morimoto, *Nat. Nanotechnol.* **2021**, *16*, 140.
14 J. Z. Li, M. J. Chen, D. A. Cullen, S. Hwang, M. Y. Wang, B. Y. Li, K. X. Liu, S. Karakalos, M. Lucero, H. G. Zhang, C. Lei, H. Xu, G. E. Sterbinsky, Z. X. Feng, D. Su, K. L. More, G. F. Wang, Z. B. Wang, G. Wu, *Nat. Catal.* **2018**, *1*, 935.
15 R. Chattot, O. L. Bacq, V. Beermann, S. Kühl, J. Herranz, S. Henning, L. Kühn, T. Asset, L. Guétaz, G. Renou, J. Drnec, P. Bordet, A. Pasturel, A. Eychmüller, T. J. Schmidt, P. Strasser, L. Dubau, F. Maillard, *Nat. Mater.* **2018**, *17*, 827.
16 X. Wan, X. F. Liu, Y. C. Li, R. H. Yu, L. R. Zheng, W. S. Yan, H. Wang, M. Xu, J. L. Shui, *Nat. Catal.* **2019**, *2*, 259.
17 X. X. Wang, M. T. Swihart, G. Wu, *Nat. Catal.* **2019**, *2*, 578.
18 S. Ott, A. Orfanidi, H. Schmies, B. Anke, H. N. Nong, J. Hübner, U. Gernert, M. Gliech, M. Lerch, P. Strasser, *Nat. Mater.* **2020**, *19*, 77.
19 J. R. Li, Z. Xi, Y. T. Pan, J. S. Spendelow, P. N. Duchesne, D. Su, Q. Li, C. Yu, Z. Y. Yin, B. Shen, Y. S. Kim, P. Zhang, S. H. Sun, *J. Am. Chem. Soc.* **2018**, *140*, 2926.
20 L. Z. Bu, S. J. Guo, X. Zhang, X. Shen, D. Su, G. Lu, X. Zhu, J. L. Yao, J. Guo, X. Q. Huang, *Nat. Commun.* **2016**, *7*, 11850.
21 Z. J. Kong, Y. Maswadeh, J. A. Vargas, S. Y. Shan, Z. P. Wu, H. Kareem, A. C. Leff, D. T. Tran, F. F. Chang, S. Yan, S. Nam, X. F. Zhao, J. M. Lee, J. Luo, S. Shastri, G. Yu, V. Petkov, C. J. Zhong, *J. Am. Chem. Soc.* **2020**, *142*, 1287.
22 M. C. Luo, Y. J. Sun, X. Zhang, Y. N. Qin, M. Q. Li, Y. J. Li, C. J. Li, Y. Yang, L. Wang, P. Gao, G. Lu, S. J. Guo, *Adv. Mater.* **2018**, *30*, 1705515.
23 C. Z. Zhu, D. Du, A. Eychmüller, Y. H. Lin, *Chem. Rev.* **2015**, *115*, 8896.
24 X. L. Tian, X. Zhao, Y. Q. Su, L. J. Wang, H. M. Wang, D. Dang, B. Chi, H. F. Liu, E. J. M. Hensen, X. W. Lou, B. Y. Xia, *Science* **2019**, *366*, 850.
25 C. Chen, Y. J. Kang, Z. Y. Huo, Z. W. Zhu, W. Y. Huang, H. L. Xin, J. D. Snyder, D. G. Li, J. A. Herron, M. Mavrikakis, M. F. Chi, K. L. More, Y. D. Li, N. M. Markovic, G. A. Somorjai, P. D. Yang, V. R. Stamenkovic, *Science* **2014**, *343*, 1339.
26 W. Li, D. D. Wang, Y. Q. Zhang, L. Tao, T. H. Wang, Y. Q. Zou, Y. Y. Wang, R. Chen, S. Y. Wang, *Adv. Mater.* **2020**, *32*, 1907879.
27 X. H. Sun, K. Z. Jiang, N. Zhang, S. J. Guo, X. Q. Huang, *ACS Nano* **2015**, *9*, 7634.
28 L. Z. Bu, B. L. Huang, Y. M. Zhu, F. D. Ning, X. C. Zhou, X. Q. Huang, *CCS Chem.* **2020**, *2*, 401.
29 H. W. Huang, K. Li, Z. Chen, L. H. Luo, Y. Q. Gu, D. Y. Zhang, C. Ma, R. Si, J. L. Yang, Z. M. Peng, J. Zeng, *J. Am. Chem. Soc.* **2017**, *139*, 8152.
30 K. Li, X. X. Li, H. W. Huang, L. H. Luo, X. Li, X. P. Yan, C. Ma, R. Si, J. L. Yang, J. Zeng, *J. Am. Chem. Soc.* **2018**, *140*, 16159.
31 J. Greeley, I. E. L. Stephens, A. S. Bondarenko, T. P. Johansson, H. A. Hansen, T. F. Jaramillo, J. Rossmeisl, I. Chorkendorff, J. K. Nørskov, *Nat. Chem.* **2009**, *1*, 552.

32 A. Kulkarni, S. Siahrostami, A. Patel, J. K. Nørskov, *Chem. Rev.* **2018**, *118*, 2302.
33 S. J. Clark, M. D. Segall, C. J. Pickard, P. J. Hasnip, M. I. J. Probert, K. Refson, M. C. Payne, *Z. Kristallogr.* **2005**, *220*, 567.
34 J. P. Perdew, K. Burke, M. Ernzerhof, *Phys. Rev. Lett.* **1996**, *77*, 3865.
35 P. J. Hasnip, C. J. Pickard, *Comput.Chevy Phys. Commun.* **2006**, *174*, 24.
36 J. P. Perdew, J. A. Chevary, V. Jackson S. H., K. A. Jackson, M. R. Pederson, J. Singh, C. Fiolhais, *Phys. Rev. B* **1992**, *46*, 6671.
37 J. D. Head, M. C. Zerner, *Chem. Phys. Lett.* **1985**, *122*, 264.